molecules

MDPI

Article

Cu_2O-Ag Tandem Catalysts for Selective Electrochemical Reduction of CO_2 to C_2 Products

Di Niu [1], Cong Wei [1], Zheng Lu [1], Yanyan Fang [1], Bo Liu [1], Da Sun [1], Xiaobin Hao [1,*], Hongge Pan [2,3] and Gongming Wang [1,*]

[1] Department of Applied Chemistry, University of Science and Technology of China, Hefei 230026, China; niudi@mail.ustc.edu.cn (D.N.); weicong@mail.ustc.edu.cn (C.W.); luzh2018@mail.ustc.edu.cn (Z.L.); fr1478@mail.ustc.edu.cn (Y.F.); liubo123@mail.ustc.edu.cn (B.L.); sunda727@mail.ustc.edu.cn (D.S.)
[2] Institute of Science and Technology for New Energy, Xi'an Technological University, Xi'an 710021, China; honggepan@zju.edu.cn
[3] State Key Laboratory of Silicon Materials, School of Materials Science and Engineering, Zhejiang University, Hangzhou 310027, China
* Correspondence: haoxb@ustc.edu.cn (X.H.); wanggm@ustc.edu.cn (G.W.); Tel.: +86-551-63601051 (G.W.)

Abstract: The electrochemical carbon dioxide reduction reaction (CO_2RR) to C_2 chemicals has received great attention. Here, we report the cuprous oxide (Cu_2O) nanocubes cooperated with silver (Ag) nanoparticles via the replacement reaction for a synergetic CO_2RR. The Cu_2O-Ag tandem catalyst exhibits an impressive Faradaic efficiency (FE) of 72.85% for C_2 products with a partial current density of 243.32 $mA \cdot cm^{-2}$. The electrochemical experiments and density functional theory (DFT) calculations reveal that the introduction of Ag improves the intermediate CO concentration on the catalyst surface and meanwhile reduces the C-C coupling reaction barrier energy, which is favorable for the synthesis of C_2 products.

Keywords: carbon dioxide reduction; cuprous oxide; silver; tandem catalyst; C_2 products

Citation: Niu, D.; Wei, C.; Lu, Z.; Fang, Y.; Liu, B.; Sun, D.; Hao, X.; Pan, H.; Wang, G. Cu_2O-Ag Tandem Catalysts for Selective Electrochemical Reduction of CO_2 to C_2 Products. *Molecules* **2021**, *26*, 2175. https://doi.org/10.3390/molecules26082175

Academic Editor: Guanglin Xia

Received: 10 March 2021
Accepted: 7 April 2021
Published: 9 April 2021

1. Introduction

Fossil fuels have been increasingly consumed since the Industrial Revolution, while substantial greenhouse gas CO_2 is inevitably emitted into the atmosphere as a byproduct, along with the severe climate change [1–3]. Nowadays, reducing the emission of CO_2 and recycling CO_2 to value-added products is becoming a significant challenge that government has to face [4–6]. It is urgent to search for a clean and efficient way to convert CO_2 to form an artificial carbon recycling [7,8]. With the rapid development of the electrochemistry and electrochemical catalysis, the electrochemical CO_2 reduction reaction (CO_2RR) to highly valuable C_2 chemicals and fuels powered by renewable energy sources [9,10] represents one of the most environmentally friendly and sustainable strategies [11,12]. However, the catalytic process involved multiple electrons transfer generally suffers from low selectivity and high overpotentials [13–16]. Therefore, developing the electrocatalysts with the high selectivity and activity has been the focus of research.

Cu-based catalysts are the most-commonly used catalysts for CO_2 reduction to C_2 products such as ethylene, ethanol and acetate, because of its unique catalytic capability stemming from the electronic structures of copper [16–19]. The regulation by means of the morphology [20–22], composition [23–26] and the chemical state [27–29] has been applied to improve the performance of Cu-based catalysts. It has been demonstrated that cuprous oxide (Cu_2O) plays a critical role in improving the selectivity toward C_2 products [30–34]. For example, in 2012, Li et al. synthesized the modified Cu electrodes by reducing Cu_2O films [30]. The thin Cu_2O layers in the electrodes exhibited higher CO_2 reduction activity than pure Cu metal. Later, Kas et al. prepared Cu_2O derived copper nanoparticles and they found the selectivity of ethylene and ethane largely depended on the parent Cu_2O film thickness [31]. The oxidized Cu catalysts prepared by Mistry et al. showed a 60% Faradaic

efficiency (FE) towards ethylene [32]. Operando characterization and experimental results show that the presence of Cu^+ is key to lowering the onset potential and enhancing ethylene selectivity. In 2017, Xiao et al. used density functional theory (DFT) calculations to research on the advantages of Cu_2O-derived electrodes [34]. The results show that Cu^+ has the ability to promote CO_2 activation and the Cu^+ and Cu^0 cooperatively improves the kinetics and thermodynamics of both CO_2 activation and CO dimerization, thereby boosting the efficiency and selectivity of CO_2RR. While Cu_2O exhibits the enhanced performance in the activity and selectivity for CO_2 reduction to C_2 products, it still cannot meet the decent selectivity and activity for the industry.

Since CO is an important reaction intermediate for the C-C coupling reaction in CO_2RR to C_2 products, increasing the near-surface CO concentration (and consequently CO surface coverage) is a key factor that can enhance the selectivity towards C_2 products [35–37]. Considering that Ag owns the ability to reduce CO_2 to produce CO [38–40], cooperating Cu_2O with Ag may be an effective strategy to improve the selectivity of C_2 products. Previous studies have reported a lot of Cu-Ag catalysts [41–45], and recently a Cu-Ag tandem catalyst was synthesized by Chen et al., which resulted in a four-fold enhancement of C_2 products formation on Cu [43]. The Ag-incorporated biphasic Cu_2O-Cu catalysts synthesized by Lee et al. reached an FE for C_2 products of 49% [44]. Later, improved FEs for ethylene and ethanol of nearly 55% and 26% were achieved using nanoporous Cu-Ag alloys [45]. While the FE of C_2 products have been improved, the activity remains low and the current densities are not high enough to meet the commercial purpose. Moreover, the reaction mechanism for converting CO_2 to C_2 products on the Cu_2O-Ag catalyst also needs to be further revealed.

In this work, we prepared Ag modified Cu_2O (Cu_2O-Ag) tandem catalysts with a size of ~50 nm by a replacement reaction for CO_2RR. The electrochemical studies reveal that introducing Ag into Cu_2O can substantially boost the generation of CO and improve the FE of C_2 products to 72.85% at −1.18 V (vs. RHE). The maximum FE of acetate reaches 15.03% at −1.18 V (vs. RHE) on the Cu_2O-Ag catalyst, which is three times higher than that of the Cu_2O catalyst at the same potential. The experiments results and DFT calculations show that high coverage of CO on the catalyst surface reduces the C-C coupling barrier energy, which is helpful in the synthesis of the C_2 products.

2. Results and Discussion

Figure 1a shows the scanning electron microscopy (SEM) image of the prepared Cu_2O-Ag catalysts, which displays uniform cubic morphology. The average size of the densely distributed nanocubes is ~50 nm. Transmission electron microscopy (TEM) image in Figure 1b shows that the Cu_2O-Ag has the regular shapes with the average edge length of 50 ± 8 nm (Figure S1a,b). The morphologies and structures of Cu_2O nanocubes (Figures S1c,d and S2a,b) are similar to that of the Cu_2O-Ag nanocubes, suggesting that the Cu_2O-Ag nanocubes preserve the original morphologies and structures of Cu_2O. Moreover, the lattice fringes of Cu_2O-Ag and Cu_2O were observed by high–resolution transmission electron microscopy (HRTEM). The interplanar spacing of 0.245 and 0.217 nm of Cu_2O-Ag is assigned to the (111) and (200) plane of Cu_2O (Figure 1b), respectively, which are also observed in the Cu_2O nanocubes (Figure S2c), further confirming that the phase of Cu_2O is preserved after adding Ag. Figure 1c and S2d exhibit the X-ray diffraction (XRD) patterns for Cu_2O-Ag and Cu_2O, respectively. Both of these catalysts exhibit similar profiles, where the diffraction peaks at 2θ = 29.6°, 36.4°, 42.3°, 61.4° and 73.5° belong to the planes of Cu_2O(110), (111), (200), (220) and (210) (JCPDS 05-0667), respectively. After introducing Ag, the new peaks at 2θ = 38.0°, 44.3°, 64.4° and 77.3° corresponding to planes of Ag(111), (200), (220) and (310) (JCPDS 04-0783) appear, indicating the formation of Ag sites in the Cu_2O-Ag catalysts. Energy dispersive X-ray spectroscopy (EDS) elemental mapping was further used to prove the existence and distribution of Ag. SEM-EDS elemental mapping images (Figure S3) confirm the existence of Cu and Ag elements, which are homogeneously distributed among the catalysts. HRTEM-EDS (Figure 1d–g) elemental mapping images

show that Ag particles exist among Cu_2O nanocubes and the particle size of Ag is smaller than that of Cu_2O nanocubes. These results clearly reveal that the Cu_2O-Ag catalyst has been prepared with separated Cu_2O nanocubes and Ag nanoparticles.

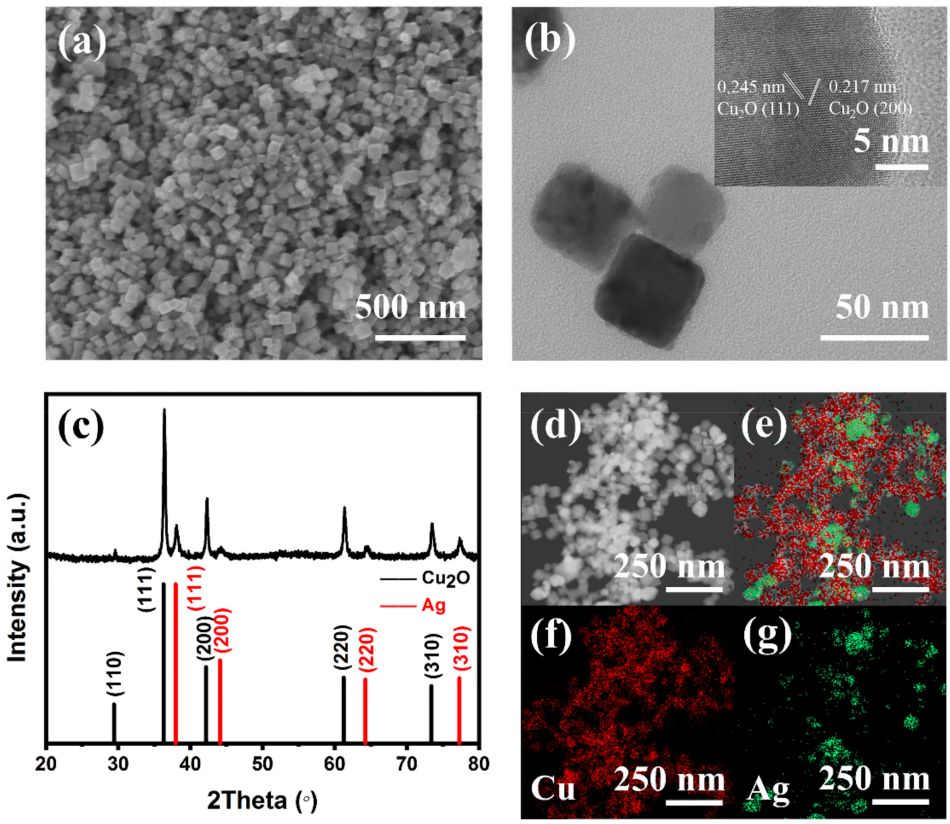

Figure 1. (**a**) SEM image of Cu_2O-Ag nanocubes. (**b**) TEM and (inset) HRTEM images of Cu_2O-Ag nanocubes. (**c**) XRD pattern of Cu_2O-Ag nanocubes. (**d**–**g**) HRTEM-EDS elemental mapping of Cu_2O-Ag nanocubes, identifying homogeneously distributed (**f**) Cu and (**g**) Ag.

The X-ray photon spectroscopy (XPS) spectrum was further conducted to probe the chemical and composition states of Cu_2O-Ag and Cu_2O catalysts. Figure 2a shows the Cu 2p spectra of Cu_2O-Ag and Cu_2O. Both catalysts display one pair of spin-orbit doublet peaks of Cu 2p, which can be assigned to Cu $2p_{3/2}$ and Cu $2p_{1/2}$, respectively. The peaks located at 932.7 and 952.5 eV are attributed to the Cu $2p_{3/2}$ and Cu $2p_{1/2}$ of the Cu_2O (Cu^+) or Cu (Cu^0), respectively [46]. After introducing Ag, the binding energies of Cu $2p_{3/2}$ and Cu $2p_{1/2}$ only exhibit a little shift to the lower energy region. It is difficult to distinguish the Cu^+ and Cu^0 chemical state through XPS because the difference of the binding energies between Cu^+ and Cu^0 is only 0.1 eV [46]. Auger electron spectroscopy (AES) was used to further verify the chemical state of Cu. Figure 2b clearly shows the signal of Cu^+ state at 569.9 eV for both samples, which is different from the metallic Cu^0 state at 568.0 eV in the reported literature [47]. The Ag $3d_{3/5}$ and $3d_{3/2}$ peaks of the Cu_2O-Ag are located at 368.6 and 374.6 eV (Figure 2c), which are consistent with the literature values of metallic Ag [48]. Furthermore, Raman spectra were also used to confirm the oxide state of Cu. In Figure 2d, both samples exhibit Raman peaks at around 219, 417, 521 and 619 cm^{-1}, which correspond to the $2\Gamma^-_{12}$, $4\Gamma^-_{12}$, Γ^+_{25} and $\Gamma^-_{12} + \Gamma^+_{25}$ phonon modes of Cu_2O [49], respectively. These results are in good agreement with the previous XRD and HRTEM measurements, confirming the formation of the Cu_2O sample and the Cu_2O-Ag tandem catalyst.

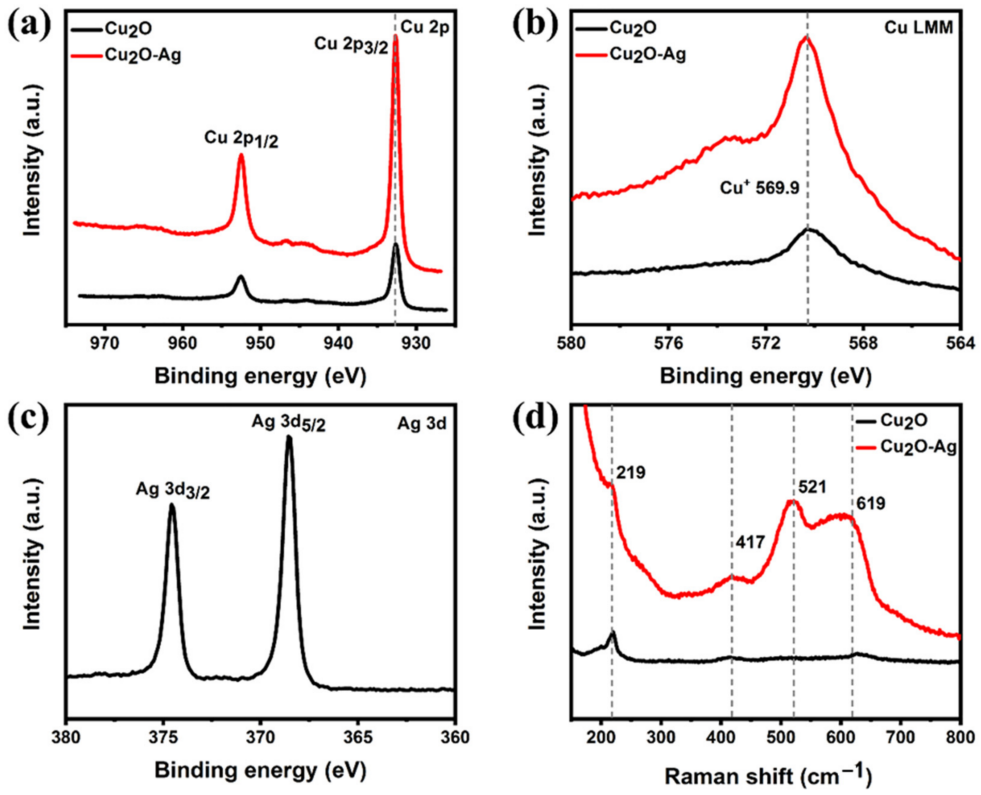

Figure 2. (**a**) XPS Cu 2p spectra. (**b**) Auger spectra of Cu LMM. And (**c**) XPS Ag 3d spectra of Cu_2O-Ag nanocubes. (**d**) Raman spectra of Cu_2O-Ag and Cu_2O nanocubes, respectively.

The selectivity and activity of CO_2RR were tested in a commercial flow-cell using gas diffusion electrode (GDE) at constant applied electrode potentials in aqueous 1 M KOH electrolyte. A cation-exchange membrane (Nafion N115, DuPont) separates the cathode compartment from the anode compartment. The catalyst powder dispersed in methanol are applied on a hydrophobic carbon paper using as the gas diffusion layer (GDL) and the GDL is used as the GDE. CO_2 is flowing through the cell at the backside of the GDL. The ambient CO_2 pressure minimizes mass transport limitations and enables high currents compared to H-type electrolytic cell test [50]. As shown in Figure 3a, the linear sweep voltammetry (LSV) curves were obtained at 10 $mV{\cdot}s^{-1}$ in 1 M KOH electrolyte on the Cu_2O-Ag and Cu_2O catalyst, respectively. Both catalysts show the sharp reduction peaks for CO_2 reduction and higher current densities compared to blank carbon paper. As the potential decreases from −0.40 to −1.15 V (vs. RHE), the total current densities of Cu_2O-Ag and Cu_2O increase from 25.31 $mA{\cdot}cm^{-2}$ to 260.80 $mA{\cdot}cm^{-2}$ and from 22.16 to 229.40 $mA{\cdot}cm^{-2}$, respectively. Therefore, the Cu_2O-Ag and Cu_2O catalysts show the similar trends in total current densities, but the current densities of Cu_2O-Ag are higher than that of Cu_2O.

The FE values of CO_2 reduction products on the Cu_2O-Ag and Cu_2O catalysts are shown in Figure 3b,c, respectively. For Cu_2O-Ag catalysts, CO and H_2 are the dominant products with total 50.01 ~ 37.57% FE at low overpotentials from −0.76 V to −0.95 V (vs. RHE). However, the FEs of CO and H_2 decrease to 10.15% and 15.92% as the potential decreases to −1.18 V (vs. RHE). Importantly, the FE of all C_2 products increases from 21.74% at −0.76 V to 72.85% at −1.18 V (vs. RHE). Ethylene and ethanol are the primary C_2 products with the FEs of 27.23% and 30.60% at −1.18 V (vs. RHE) (Figure 3d), respectively. The FE of acetate also increases from 3.90% to 15.02% as the potential decreases from −0.76 V to −1.18 V (vs. RHE) (Figure 3d). Compared with the Cu_2O-Ag catalyst, the Cu_2O catalyst shows slightly lower FE of CO and higher FE of H_2, ranging from 28.81% and 21.04% at −0.75 V to 6.86% and 17.43% at −1.18 V (vs. RHE), respectively, while the FEs of

ethylene, ethanol and acetate increase from 15.95%, 9.74% and 1.01% at −0.75 V to 30.55%, 25.84% and 5.18% at −1.18 V (vs. RHE) (Figure 3d), respectively. While the FEs of all C_2 products increases from 26.70% at −0.75 V to 61.57% at −1.18 V (vs. RHE), which shows a similar trend to the Cu_2O-Ag catalyst, the Cu_2O-Ag catalyst has the higher FE of C_2 products and lower FE of H_2.

Furthermore, as shown in Figure 3d,e, the Cu_2O-Ag catalyst reaches a maximum C_2 products FE of 72.85% at −1.18 V (vs. RHE) with the partial current density of 243.32 mA·cm^{-2}, involving 27.23% ethylene, 30.60% ethanol and 15.02% acetate. Compared to Cu_2O-Ag, the total C_2 products FE of Cu_2O is 61.57% with the partial current density of 205.64 mA·cm^{-2}, involving 30.55% ethylene, 25.84% ethanol and only 5.18% acetate. Obviously, the FE of acetate on the Cu_2O-Ag is about three times higher than that on the Cu_2O, suggesting a more prominent ability of Cu_2O-Ag than Cu_2O for CO_2 reduction to acetate.

The stability of the Cu_2O-Ag catalyst was tested at −1.18 V (vs. RHE) (Figure 3f). The catalyst shows a good performance without the decay of the current density and C_2 product FEs in 40 min. The FEs of ethanol and acetate remain over 30% and 15% for over 2400 s with a total current density of over 300 mA cm^{-2}. As shown in Figures S4 and S5, the catalyst morphology and crystal facet were changed at 5 min after CO_2RR and continuously changed with the reaction progress, while the performance is basically unchanged. Hence, the change in catalyst morphology and crystal facet might not be the main reason of performance degradation and the decrease of C_2 products FE and the current density may be due to the loss of hydrophobicity over the GDLs and the salinization of electrolyte [51–54]. From the above results, it can be concluded that the Cu_2O-Ag is more active and selective for CO_2RR to C_2 products than the Cu_2O catalyst, especially producing acetate.

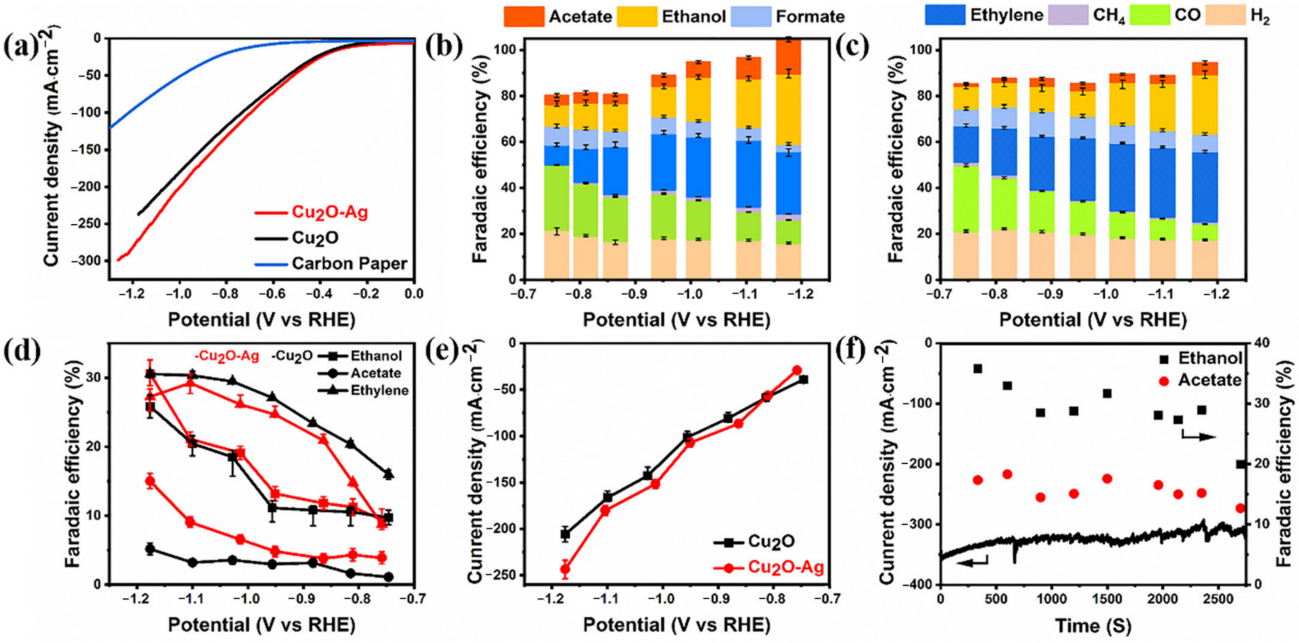

Figure 3. (**a**) LSV curves on the Cu_2O-Ag and Cu_2O nanocubes in 1 M KOH electrolytes. Blue curves obtained from the blank GDL in 1 M KOH electrolytes. (**b**) Faradaic efficiencies of all CO_2RR products on the Cu_2O-Ag nanocubes. (**c**) Faradaic efficiencies of all CO_2RR products on the Cu_2O nanocubes. (**d**) Faradaic efficiencies of ethylene, acetate and ethanol of Cu_2O-Ag and Cu_2O nanocubes at different applied potentials. (**e**) Partial current densities of C_2 products of Cu_2O-Ag and Cu_2O nanocubes at different applied potentials. (**f**) Stability test in 1M KOH electrolytes at −1.18 V versus RHE.

After the CO_2RR test, SEM and XRD were used to probe the change of morphologies and compositions of both catalysts. The SEM images show that the morphologies of Cu_2O in both Cu_2O-Ag and Cu_2O catalyst are changed to irregular particles after the

catalytic reaction (Figure S6). Small nanocubes agglomerate together to form larger and irregular shape particles under the negative potential conditions with a particle size of over 100 nm and each particle can be clearly distinguished from others. At the negative potentials, the Cu_2O is easily reduced [55]. As shown in Figure S7, the new peaks at 43.2° and 50.3° corresponding to Cu (JCPDS 04-0836) in XRD patterns are showed, indicating that most of Cu_2O is reduced to Cu after CO_2RR. However, Ag peaks and Cu_2O peaks are still existed in XRD patterns, which means that Ag and a small amount of Cu_2O are preserved after CO_2RR. EDS elemental mapping (Figure S8a–c) also confirms that Ag still exists and is homogeneously distributed on the GDL. The content of Ag investigated by inductively coupled plasma-atomic emission spectrometry (ICP-AES) decreases from 9.72% to 7.39% after CO_2RR (Table S1). The reason for the decreased Ag content might be that it is flushed away by electrolytes. XPS results of Cu_2O-Ag after CO_2RR in Figure S9 show the characteristic metallic Ag peaks and mixed Cu^0 + Cu^+ peaks, confirming the existence of Ag and reduction of Cu_2O to Cu, and the XPS spectrum of Cu_2O after CO_2RR also shows the mixed Cu^0 + Cu^+ peaks (Figure S10) [56–58].

In order to investigate the mechanism of higher FEs of C_2 products, the following experiments are further studied. As shown in Figure 3, the introduction of Ag promotes producing C_2 products. The FE of acetate increases as the mass ratios of Ag increase (Figure S11). When Ag is introduced into Cu_2O, it acts as the CO active site, creating a high surface concentration of CO, which benefits CO dimerization and the synthesis of C_2 products [59]. The produced CO can be transferred neighboring Cu, along with C-C coupling reaction to produce C_2 products, which results in the highly selective CO dimerization. Moreover, a higher CO concentration also benefits from increasing the reaction rate of the C-C coupling step and FEs of C_2 products. As shown in Figure 4a,b, the Cu_2O-Ag catalyst produces more CO at high overpotentials than Cu_2O, corresponding to the increases of acetate FE. At the potential of −1.18 V (vs. RHE), the FE of CO for Cu_2O-Ag catalyst is 10.15%, corresponding to 15.02% acetate. In contrast, the Cu_2O catalyst produce 6.86% FE of CO, corresponding to 5.18% FE of acetate. These experimental results show that the FE of CO is related to that of acetate and a high CO concentration may be helpful to the synthesis of C_2 products, which is further revealed by the following DFT calculations.

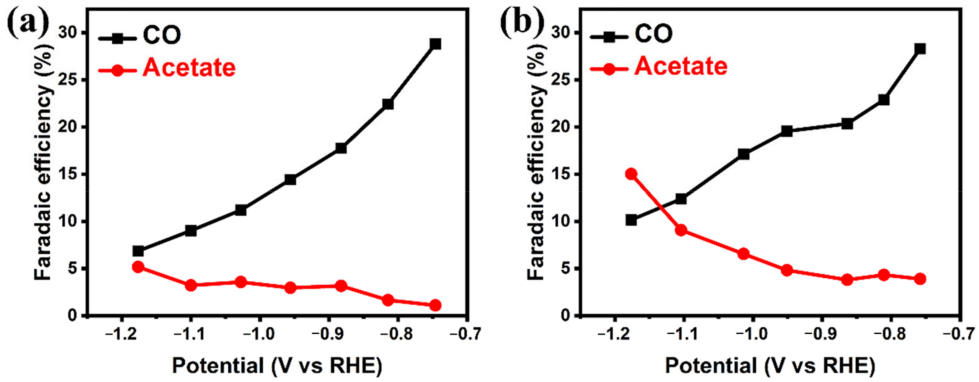

Figure 4. CO and acetate Faradaic efficiencies on (**a**) Cu_2O and (**b**) Cu_2O-Ag nanocubes at different applied potentials.

Cu_2O and Ag are regarded as an important active site for converting CO_2 to CO [34,60]. Therefore, in our study, not only Cu_2O, but also Ag, can act as active sites producing CO from CO_2. More CO can react with each other on Cu surface to form C-C bond and further C_2 product. DFT calculations were applied to investigate the effect of CO coverage on the C-C coupling step over the Cu catalyst, which is the key fundamental step for the synthesis of C_2 products. Considering the reduction of Cu_2O to Cu during the CO_2 reduction process, the Cu surface, with the (100) plane having the $p(3 \times 3)$ size, was constructed to model the catalyst [61]. The most stable adsorption site of CO on Cu(100) surface is firstly explored. As shown in Figure S12, CO is preferred to adsorb at the bridge site, which accords well

with the previous study [62]. In order to model the effect of the high CO concentration on Cu producing and spilling from Ag, we compared the reaction barrier energies of the C-C coupling step at the CO coverage of 3/9 ML with 2/9 ML, which represents the high and low CO concentration on the catalyst surface, respectively. As shown in Figure 5, there is the lower C-C coupling barrier energy (1.10 eV) on 3/9 ML than that (1.63 eV) on 2/9 ML, which indicates that the high coverage of CO promotes the C-C coupling step and the C_2 products. However, the barrier energy of C-C coupling reaction on the $p(2 \times 2)$ $Cu_2O(100)$ surface (3.03 eV) at the CO coverage of 1/2 ML is much higher than those on the Cu surface at different coverages (1.63 and 1.10 eV) (Figure S13), which suggests that Cu is more favorable for the C-C coupling reaction than Cu_2O.

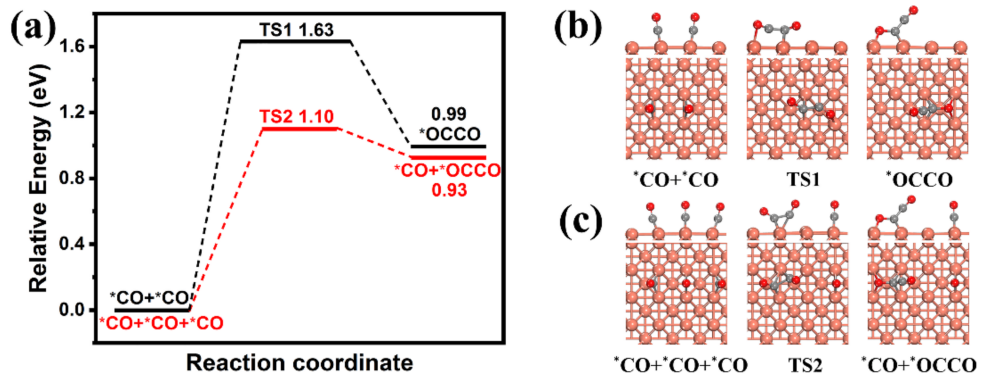

Figure 5. (**a**) Reaction barrier energies of C-C coupling step at the low and high CO concentrations; the corresponding configurations of initial state, transition state and final state on the CO coverage of (**b**) 2/9 ML and (**c**) 3/9 ML. Light red, copper; grey, carbon; red, oxygen; TS, transition state; * represents adsorbates).

3. Materials and Methods

3.1. Materials

Copper sulfate ($CuSO_4 \cdot 5H_2O$, 99%), sodium hydroxide (NaOH, 99%), ascorbic acid ($C_6H_8O_6$, 99.7%) and silver nitrate ($AgNO_3$, 99.95%) were purchased from Shanghai Sinopharm Chemical Reagent Co., Ltd. (Shanghai, China) and were used without purification.

3.2. Synthesis of Cu_2O Nanocubes

The Cu_2O nanocubes were synthesized by a previously reported method [63]. In a typical synthesis, 0.3 g $CuSO_4 \cdot 5H_2O$ was dissolved in 400 mL deionized water (DIW) and stirred for 30 min at 20 °C. Then, 1 mL 4.8 M NaOH solution was added slowly. After 5 min, 1 mL 1.2 M ascorbic acid was injected. The solution was further stirred for 30 min and the solution color was turned from blue to orange. The sample was washed with DIW and ethanol at least 3 times, respectively. Then, it was dried at 60 °C in a vacuum oven overnight.

3.3. Synthesis of Cu_2O-Ag Nanocubes

The Cu_2O nanocubes were synthesized following the above-mentioned steps. After the Cu_2O nanocubes solution was prepared, a certain amount of silver nitrate solution (35 mL, 2 mmol) was injected. The solution color was turned from orange to black immediately and then stirred for 5 min. The sample was washed with DIW and ethanol at least 3 times. Then, it was dried at 60 °C in a vacuum oven overnight.

3.4. Material Characterizations

The prepared samples were characterized by the following techniques. X-ray diffraction (XRD) measurements were performed on a Philips X'Pert Pro Super diffractometer (Philips, Almelo, The Netherlands) using Cu Kα radiation (λ = 1.54178 Å). The morpholog-

ical structures were collected using a JEOL-2010-JSM-6700F scanning electron microscopy (SEM) (JEOL, Tokyo, Japan) and Hitachi H7650 transmission electron microscopy (TEM) (Hitachi, Tokyo, Japan). Energy dispersive X-ray spectroscopy (EDS) mapping and high–resolution transmission electron microscopy (HRTEM) images were acquired on Talos F200X (FEI, Hillsboro, OR, USA) and JEMARM 200F microscope (JEOL, Tokyo, Japan). Raman spectra were recorded on a Renishaw RM 3000 Micro-Raman system (Renishaw, Gloucestershire, UK) with a 532 nm excitation laser. X-ray photon spectroscopy (XPS) and Auger electron spectroscopy (AES) were performed at Thermo Scientific ESCALAB 250Xi X-ray Photoelectron Spectrometer (Thermo, Waltham, MA, USA).

3.5. Electrochemical Measurements

All the electrochemical measurements were performed in a three-electrode system on CHI 760E electrochemical workstation (Chenhua, Shanghai, China). The potentials were measured against an Ag/AgCl reference electrode and converted to the reversible hydrogen electrode (RHE) using the equation:

$$E \text{ (vs. RHE)} = E \text{ (vs. Ag/AgCl)} + 0.197 + (0.059 \times \text{pH}) \quad (1)$$

A gas diffusion layer (GDL) was used as the catalyst support. We dispersed 5 mg catalyst powder in 1 mL methanol and 40 µL 5 wt% Nafion. The ink was sonicated for 30 min and dripped on the top of GDL (1 cm^2). Then, the GDL was dried in a vacuum oven at 60 °C for 4 h. The GDL was weighed before and after catalyst deposition and loading contents were 1 mg cm^{-2}.

The electrolysis investigations were carried out in a flow cell purchased from Gaossunion (Gaossunion, Wuhan, China). The cathode (GDL) and anode (nickel foam) compartments were separated by an anion exchange membrane. The CO_2 gas chamber was located behind the cathode chamber and separated from the catholyte with a GDL. The CO_2 flow rates were set at 20 mL min^{-1}. Electrolytes were circulated through cathode and anode through the cell at 10 mL min^{-1} using peristaltic pump. 1 M KOH (25 mL) was used as electrolyte solutions. All electrolyte solutions were prepared with deionized water (18.2 MΩ cm).

3.6. Product Analysis

Gas and liquid products were quantified by gas chromatography (GC) (GC9560, Awa, Shanghai, China) and nuclear magnetic resonance (NMR) spectroscopy (AVANCE 400, Bruker, Fällanden, Switzerland), respectively. Faradaic efficiencies (FE) of gas and liquid products were calculated using the following equation:

$$\text{FE (\%)} = eFn/Q \times 100\% = eFn/It \times 100\% \quad (2)$$

where e is the number of electrons transferred, F is the Faraday constant, n is the amount of product in moles, Q is the charge, I is the current and t is the electrolysis time.

3.7. Theoretical Calculation

Density functional theory (DFT) calculation, performed by the Vienna Ab-initio Simulation Package (VASP 5.3) code (University of Vienna, Vienna, Austria), was used in this study [64–66]. The electron exchange-correlation potential was conducted by the Perdew-Burke-Ernzerhof (PBE) functional of generalized gradient approximation (GGA) [67,68]. The kinetic energy cut-off energy was set to 520 eV for the plane-wave basis set and the DFT dispersion correction (DFT-D3) [69] method was used to treat the van der Waals interactions. Brillouin zone integration was sampled with the 9 × 9 × 9 and 3 × 3 × 1 Monkhorst-Pack mesh k-point for bulk and surface calculations, respectively. The convergence of geometric optimization was checked with the forces less than 0.01 eV·$Å^{-1}$ and the energy difference less than 1×10^{-5} eV. The climbing-image nudged elastic band method (CI-NEB) [70,71] was employed to obtain the approximate transition statessaddle point, followed by the

dimer method [72], which was carried out to further optimize the transition states with the convergence criteria of the force acting on the atom less than 0.05 eV Å. Meanwhile, the transition state was verified using the single imaginary frequency. In addition, a U-J value of 3 eV was used for DFT+U correction on the $Cu_2O(100)$ surface. The adsorption energy (E_{ads}), activation energy (E_a) and reaction energy (ΔE) were obtained by the formulas:

$$E_{ads} = E_{CO/substrate} - E_{CO} - E_{substrate} \quad (3)$$

$$E_a = E_{TS} - E_{IS} \quad (4)$$

$$\Delta E = E_{FS} - E_{IS} \quad (5)$$

where E_{ads} is the adsorption energy of *CO on the surface, $E_{CO/substrate}$ is the total energy of substrate and CO, E_{CO} is the energy of CO, $E_{substrate}$ is the energy of substrate; E_a and ΔE are the barrier and the reaction energy, respectively; E_{IS}, E_{TS} and E_{FS} are the energy of initial state, transition state and final state, respectively.

4. Conclusions

In summary, we prepared a Cu_2O-Ag tandem catalyst for CO_2 electrochemical reduction reaction through a facile synthetic method. The tandem catalyst made up of Cu_2O and Ag nanoparticles improves the selectivity and activity of CO_2 reduction toward C_2 products compared to Cu_2O catalyst. At the potential of -1.18 V (vs. RHE), the Cu_2O-Ag catalyst shows a maximum C_2 products FE of 72.85% with a partial current density of -243.32 mA·cm^{-2}. It has an FE of 15.02% towards acetate, which is three times higher than that of Cu_2O. Based on further experiments and DFT calculation, we found that increased CO concentration, produced on the Ag sites, plays an important role towards the production of acetate. The study shows a simple method to improve C_2 production and provides deeper insights into designing the catalysts for CO_2 electrochemical reduction.

Supplementary Materials: The following data are available online, Figure S1. (a) TEM image and (b) size distribution of Cu_2O-Ag nanocubes; (c) TEM image and (d) size distribution of Cu_2O nanocubes. Figure S2. (a) SEM image of Cu_2O nanocubes; (b) TEM image of Cu_2O nanocubes; (c) HRTEM image of Cu_2O nanocubes; (d) XRD pattern of Cu_2O nanocubes. Figure S3. (a–c) SEM-EDS elemental mapping of Cu_2O-Ag nanocubes, showing the distribution of elemental (b) Cu and (c) Ag within the particles. Figure S4. The SEM images of the Cu_2O-Ag during CO_2RR. (a) 0 min, (b) 5 min, (c) 10 min, (d) 15 min, (e) 20 min, (f) 25 min, (g) 30 min, (h) 35 min, (i) 40 min. Scale bar = 500 nm. Figure S5. The XRD pattrens of the Cu_2O-Ag during CO_2RR. Figure S6. SEM images of (a) Cu_2O-Ag nanocubes and (b) Cu_2O nanocubes after CO_2RR. Figure S7. XRD patterns of (a) Cu_2O-Ag nanocubes and (b) Cu_2O nanocube after CO_2RR. Figure S8. (a–c) SEM-EDS elemental mapping of Cu_2O-Ag nanocubes of elemental (b) Cu and (c) Ag after CO_2RR. Table S1. Cu and Ag contents of Cu_2O-Ag nanocubes before and after CO_2RR. Figure S9. XPS spectra for (a) Cu and (b) Ag of Cu_2O-Ag nanocubes after CO_2RR. Figure S10. XPS spectra for Cu of Cu_2O nanocubes after CO_2RR. Figure S11. Faradaic efficiency of acetate of the different mass ratios of Ag in the Cu_2O-Ag nanocubes. Figure S12. Adsorption energy and corresponding configuration of CO at three type sites on Cu(100) surface. Figure S13. (a) Reaction energy barrier diagram of the C-C coupling step on the $Cu_2O(100)$ surface with the (b)corresponding configurations of two *CO forming an *OCCO. Light red, copper; grey, carbon; red, oxygen; TS, transition state.

Author Contributions: Experimental design and implementation, D.N. and G.W.; DFT calculation design and implementation, C.W. and X.H.; data analysis, D.N., Z.L. and Y.F.; characterization, D.N., B.L. and D.S.; writing—original draft preparation, D.N. and C.W.; writing—reviewing and editing, D.N. and X.H.; supervision G.W. and H.P.; All authors contributed to discussion of the results and manuscript preparation. All authors have read and agreed to the published version of the manuscript.

Funding: The research is supported by the Natural Science Fund of China (21771169), the National Key Research and Development Program of China (2017YFA0206703), Anhui Provincial Natural Science Foundation (BJ2060190077), the Fundamental Research Funds for the Central Universities (WK2060000015), and the Collaborative Innovation program of Hefei Science Center, CAS.

Institutional Review Board Statement: Not applicable.

Informed Consent Statement: Not applicable.

Data Availability Statement: The data presented in this study are available in the article and supplementary material.

Acknowledgments: All authors are very thankful to the support from Natural Science Fund of China and other funds. All authors also thank the Supercomputing Center of University of Science and Technology of China.

Conflicts of Interest: The authors declare no conflict of interest. The funders had no role in the design of the study; in the collection, analyses, or interpretation of data; in the writing of the manuscript, or in the decision to publish the results.

Sample Availability: Samples of the compound are available from the authors.

References

1. Baker, H.S.; Millar, R.J.; Karoly, D.J.; Beyerle, U.; Guillod, B.P.; Mitchell, D.; Shiogama, H.; Sparrow, S.; Woollings, T.; Allen, M.R. Higher CO_2 concentrations increase extreme event risk in a 1.5 °C world. *Nat. Clim. Change* **2018**, *8*, 604–608. [CrossRef]
2. Rogelj, J.; Huppmann, D.; Krey, V.; Riahi, K.; Clarke, L.; Gidden, M.; Nicholls, Z.; Meinshausen, M. A new scenario logic for the Paris Agreement long-term temperature goal. *Nature* **2019**, *573*, 357–363. [CrossRef] [PubMed]
3. Shakun, J.D.; Clark, P.U.; He, F.; Marcott, S.A.; Mix, A.C.; Liu, Z.; Otto-Bliesner, B.; Schmittner, A.; Bard, E. Global warming preceded by increasing carbon dioxide concentrations during the last deglaciation. *Nature* **2012**, *484*, 49–54. [CrossRef] [PubMed]
4. Montzka, S.A.; Dlugokencky, E.J.; Butler, J.H. Non-CO_2 greenhouse gases and climate change. *Nature* **2011**, *476*, 43–50. [CrossRef] [PubMed]
5. Rogelj, J.; McCollum, D.L.; O'Neill, B.C.; Riahi, K. 2020 emissions levels required to limit warming to below 2 °C. *Nat. Clim. Change* **2012**, *3*, 405–412. [CrossRef]
6. Tavoni, M.; Kriegler, E.; Riahi, K.; van Vuuren, D.P.; Aboumahboub, T.; Bowen, A.; Calvin, K.; Campiglio, E.; Kober, T.; Jewell, J.; et al. Post-2020 climate agreements in the major economies assessed in the light of global models. *Nat. Clim. Change* **2014**, *5*, 119–126. [CrossRef]
7. Bushuyev, O.S.; De Luna, P.; Dinh, C.T.; Tao, L.; Saur, G.; van de Lagemaat, J.; Kelley, S.O.; Sargent, E.H. What should we make with CO_2 and how can we make it? *Joule* **2018**, *2*, 825–832. [CrossRef]
8. Olah, G.A.; Prakash, G.K.; Goeppert, A. Anthropogenic chemical carbon cycle for a sustainable future. *J. Am. Chem. Soc.* **2011**, *133*, 12881–12898. [CrossRef]
9. Barnhart, C.J.; Dale, M.; Brandt, A.R.; Benson, S.M. The energetic implications of curtailing versus storing solar- and wind-generated electricity. *Energy Environ. Sci.* **2013**, *6*, 2804–2810. [CrossRef]
10. Brouwer, A.S.; van den Broek, M.; Seebregts, A.; Faaij, A. Impacts of large-scale Intermittent Renewable Energy Sources on electricity systems, and how these can be modeled. *Renew. Sustain. Energy Rev.* **2014**, *33*, 443–466. [CrossRef]
11. Chu, S.; Cui, Y.; Liu, N. The path towards sustainable energy. *Nat. Mater.* **2016**, *16*, 16–22. [CrossRef]
12. Kondratenko, E.V.; Mul, G.; Baltrusaitis, J.; Larrazábal, G.O.; Pérez-Ramírez, J. Status and perspectives of CO_2 conversion into fuels and chemicals by catalytic, photocatalytic and electrocatalytic processes. *Energy Environ. Sci.* **2013**, *6*, 3112–3135. [CrossRef]
13. Birdja, Y.Y.; Pérez-Gallent, E.; Figueiredo, M.C.; Göttle, A.J.; Calle-Vallejo, F.; Koper, M.T.M. Advances and challenges in understanding the electrocatalytic conversion of carbon dioxide to fuels. *Nat. Energy* **2019**, *4*, 732–745. [CrossRef]
14. Jones, J.-P.; Prakash, G.K.S.; Olah, G.A. Electrochemical CO_2 reduction: Recent advances and current trends. *Isr. J. Chem.* **2014**, *54*, 1451–1466. [CrossRef]
15. Kibria, M.G.; Edwards, J.P.; Gabardo, C.M.; Dinh, C.T.; Seifitokaldani, A.; Sinton, D.; Sargent, E.H. Electrochemical CO_2 reduction into chemical feedstocks: From mechanistic electrocatalysis models to system design. *Adv. Mater.* **2019**, *31*, 1807166. [CrossRef]
16. Gao, D.; Arán-Ais, R.M.; Jeon, H.S.; Roldan Cuenya, B. Rational catalyst and electrolyte design for CO_2 electroreduction towards multicarbon products. *Nat. Catal.* **2019**, *2*, 198–210. [CrossRef]
17. Nitopi, S.; Bertheussen, E.; Scott, S.B.; Liu, X.; Engstfeld, A.K.; Horch, S.; Seger, B.; Stephens, I.E.L.; Chan, K.; Hahn, C.; et al. Progress and perspectives of electrochemical CO_2 reduction on copper in aqueous electrolyte. *Chem. Rev.* **2019**, *119*, 7610–7672. [CrossRef]
18. Qiao, J.; Liu, Y.; Hong, F.; Zhang, J. A review of catalysts for the electroreduction of carbon dioxide to produce low-carbon fuels. *Chem. Soc. Rev.* **2014**, *43*, 631–675. [CrossRef]
19. Raciti, D.; Wang, C. Recent advances in CO_2 reduction electrocatalysis on copper. *ACS Energy Lett.* **2018**, *3*, 1545–1556. [CrossRef]
20. De Luna, P.; Quintero-Bermudez, R.; Dinh, C.-T.; Ross, M.B.; Bushuyev, O.S.; Todorović, P.; Regier, T.; Kelley, S.O.; Yang, P.; Sargent, E.H. Catalyst electro-redeposition controls morphology and oxidation state for selective carbon dioxide reduction. *Nat. Catal.* **2018**, *1*, 103–110. [CrossRef]
21. Kim, J.; Choi, W.; Park, J.W.; Kim, C.; Kim, M.; Song, H. Branched copper oxide nanoparticles induce highly selective ethylene production by electrochemical carbon dioxide reduction. *J. Am. Chem. Soc.* **2019**, *141*, 6986–6994. [CrossRef]

22. Wang, Y.; Shen, H.; Livi, K.J.T.; Raciti, D.; Zong, H.; Gregg, J.; Onadeko, M.; Wan, Y.; Watson, A.; Wang, C. Copper nanocubes for CO_2 reduction in gas diffusion electrodes. *Nano Lett.* **2019**, *19*, 8461–8468. [CrossRef]
23. Chen, X.; Henckel, D.A.; Nwabara, U.O.; Li, Y.; Frenkel, A.I.; Fister, T.T.; Kenis, P.J.A.; Gewirth, A.A. Controlling speciation during CO_2 reduction on Cu-alloy electrodes. *ACS Catal.* **2019**, *10*, 672–682. [CrossRef]
24. Ma, S.; Sadakiyo, M.; Heima, M.; Luo, R.; Haasch, R.T.; Gold, J.I.; Yamauchi, M.; Kenis, P.J. Electroreduction of carbon dioxide to hydrocarbons using bimetallic Cu-Pd catalysts with different mixing patterns. *J. Am. Chem. Soc.* **2017**, *139*, 47–50. [CrossRef]
25. Ren, D.; Ang, B.S.-H.; Yeo, B.S. Tuning the selectivity of carbon dioxide electroreduction toward ethanol on oxide-derived Cu_xZn catalysts. *ACS. Catal.* **2016**, *6*, 8239–8247. [CrossRef]
26. Zhou, Y.; Che, F.; Liu, M.; Zou, C.; Liang, Z.; De Luna, P.; Yuan, H.; Li, J.; Wang, Z.; Xie, H.; et al. Dopant-induced electron localization drives CO_2 reduction to C_2 hydrocarbons. *Nat. Chem.* **2018**, *10*, 974–980. [CrossRef]
27. Chou, T.C.; Chang, C.C.; Yu, H.L.; Yu, W.Y.; Dong, C.L.; Velasco-Velez, J.J.; Chuang, C.H.; Chen, L.C.; Lee, J.F.; Chen, J.M.; et al. Controlling the oxidation state of the Cu electrode and reaction intermediates for electrochemical CO_2 reduction to ethylene. *J. Am. Chem. Soc.* **2020**, *142*, 2857–2867. [CrossRef]
28. Ren, D.; Deng, Y.; Handoko, A.D.; Chen, C.S.; Malkhandi, S.; Yeo, B.S. Selective electrochemical reduction of carbon dioxide to ethylene and ethanol on copper(I) oxide catalysts. *ACS. Catal.* **2015**, *5*, 2814–2821. [CrossRef]
29. Yang, P.P.; Zhang, X.L.; Gao, F.Y.; Zheng, Y.R.; Niu, Z.Z.; Yu, X.; Liu, R.; Wu, Z.Z.; Qin, S.; Chi, L.P.; et al. Protecting copper oxidation state via intermediate confinement for selective CO_2 electroreduction to C_{2+} fuels. *J. Am. Chem. Soc.* **2020**, *142*, 6400–6408. [CrossRef] [PubMed]
30. Li, C.W.; Kanan, M.W. CO_2 reduction at low overpotential on Cu electrodes resulting from the reduction of thick Cu_2O films. *J. Am. Chem. Soc.* **2012**, *134*, 7231–7234. [CrossRef] [PubMed]
31. Kas, R.; Kortlever, R.; Milbrat, A.; Koper, M.T.; Mul, G.; Baltrusaitis, J. Electrochemical CO_2 reduction on Cu_2O-derived copper nanoparticles: Controlling the catalytic selectivity of hydrocarbons. *Phys. Chem. Chem. Phys.* **2014**, *16*, 12194–12201. [CrossRef]
32. Li, C.W.; Ciston, J.; Kanan, M.W. Electroreduction of carbon monoxide to liquid fuel on oxide-derived nanocrystalline copper. *Nature* **2014**, *508*, 504–507. [CrossRef]
33. Mistry, H.; Varela, A.S.; Bonifacio, C.S.; Zegkinoglou, I.; Sinev, I.; Choi, Y.W.; Kisslinger, K.; Stach, E.A.; Yang, J.C.; Strasser, P.; et al. Highly selective plasma-activated copper catalysts for carbon dioxide reduction to ethylene. *Nat. Commun.* **2016**, *7*, 12123. [CrossRef]
34. Xiao, H.; Goddard, W.A., III; Cheng, T.; Liu, Y. Cu metal embedded in oxidized matrix catalyst to promote CO_2 activation and CO dimerization for electrochemical reduction of CO_2. *Proc. Natl. Acad. Sci. USA* **2017**, *114*, 6685–6688. [CrossRef]
35. Li, J.; Wang, Z.; McCallum, C.; Xu, Y.; Li, F.; Wang, Y.; Gabardo, C.M.; Dinh, C.-T.; Zhuang, T.-T.; Wang, L.; et al. Constraining CO coverage on copper promotes high-efficiency ethylene electroproduction. *Nat. Catal.* **2019**, *2*, 1124–1131. [CrossRef]
36. Morales-Guio, C.G.; Cave, E.R.; Nitopi, S.A.; Feaster, J.T.; Wang, L.; Kuhl, K.P.; Jackson, A.; Johnson, N.C.; Abram, D.N.; Hatsukade, T.; et al. Improved CO_2 reduction activity towards C_{2+} alcohols on a tandem gold on copper electrocatalyst. *Nat. Catal.* **2018**, *1*, 764–771. [CrossRef]
37. Wang, X.; de Araujo, J.F.; Ju, W.; Bagger, A.; Schmies, H.; Kuhl, S.; Rossmeisl, J.; Strasser, P. Mechanistic reaction pathways of enhanced ethylene yields during electroreduction of CO_2-CO co-feeds on Cu and Cu-tandem electrocatalysts. *Nat. Nanotechnol.* **2019**, *14*, 1063–1070. [CrossRef]
38. Ham, Y.S.; Choe, S.; Kim, M.J.; Lim, T.; Kim, S.-K.; Kim, J.J. Electrodeposited Ag catalysts for the electrochemical reduction of CO_2 to CO. *Appl. Catal. B Environ.* **2017**, *208*, 35–43. [CrossRef]
39. Sun, K.; Wu, L.; Qin, W.; Zhou, J.; Hu, Y.; Jiang, Z.; Shen, B.; Wang, Z. Enhanced electrochemical reduction of CO_2 to CO on Ag electrocatalysts with increased unoccupied density of states. *J. Mater. Chem. A* **2016**, *4*, 12616–12623. [CrossRef]
40. Mahyoub, S.A.; Qaraah, F.A.; Chen, C.; Zhang, F.; Yan, S.; Cheng, Z. An overview on the recent developments of Ag-based electrodes in the electrochemical reduction of CO_2 to CO. *Sustain. Energy Fuels* **2020**, *4*, 50–67. [CrossRef]
41. Martić, N.; Reller, C.; Macauley, C.; Löffler, M.; Reichert, A.M.; Reichbauer, T.; Vetter, K.-M.; Schmid, B.; McLaughlin, D.; Leidinger, P.; et al. $Ag_2Cu_2O_3$—A catalyst template material for selective electroreduction of CO to C_{2+} products. *Energy Environ. Sci.* **2020**, *13*, 2993–3006. [CrossRef]
42. Wang, Y.; Wang, D.; Dares, C.J.; Marquard, S.L.; Sheridan, M.V.; Meyer, T.J. CO_2 reduction to acetate in mixtures of ultrasmall $(Cu)_n$,$(Ag)_m$ bimetallic nanoparticles. *Proc. Natl. Acad. Sci. USA* **2018**, *115*, 278–283. [CrossRef]
43. Chen, C.; Li, Y.; Yu, S.; Louisia, S.; Jin, J.; Li, M.; Ross, M.B.; Yang, P. Cu-Ag tandem catalysts for high-rate CO_2 electrolysis toward multicarbons. *Joule* **2020**, *4*, 1688–1699. [CrossRef]
44. Lee, S.; Park, G.; Lee, J. Importance of Ag–Cu biphasic boundaries for selective electrochemical reduction of CO_2 to ethanol. *ACS. Catal.* **2017**, *7*, 8594–8604. [CrossRef]
45. Hoang, T.T.H.; Verma, S.; Ma, S.; Fister, T.T.; Timoshenko, J.; Frenkel, A.I.; Kenis, P.J.A.; Gewirth, A.A. Nanoporous copper-silver alloys by additive-controlled electrodeposition for the selective electroreduction of CO_2 to ethylene and ethanol. *J. Am. Chem. Soc.* **2018**, *140*, 5791–5797. [CrossRef]
46. Ghodselahi, T.; Vesaghi, M.A.; Shafiekhani, A.; Baghizadeh, A.; Lameii, M. XPS study of the $Cu@Cu_2O$ core-shell nanoparticles. *Appl. Surf. Sci.* **2008**, *255*, 2730–2734. [CrossRef]

47. Jung, H.; Lee, S.Y.; Lee, C.W.; Cho, M.K.; Won, D.H.; Kim, C.; Oh, H.S.; Min, B.K.; Hwang, Y.J. Electrochemical fragmentation of Cu_2O nanoparticles enhancing selective C-C coupling from CO_2 reduction reaction. *J. Am. Chem. Soc.* **2019**, *141*, 4624–4633. [CrossRef]
48. Sun, D.; Li, P.; Yang, B.; Xu, Y.; Huang, J.; Li, Q. Monodisperse AgPd alloy nanoparticles as a highly active catalyst towards the methanolysis of ammonia borane for hydrogen generation. *RSC. Adv.* **2016**, *6*, 105940–105947. [CrossRef]
49. Yu, P.Y.; Shen, Y.R. Resonance Raman studies in Cu_2O. I. the phonon-assisted 1s yellow excitonic absorption edge. *Phys. Rev. B* **1975**, *12*, 1377–1394. [CrossRef]
50. Ren, S.; Joulie, D.; Salvatore, S.; Torbensen, K.; Wang, M.; Robert, M.; Beilinguette, C.P. Molecular electrocatalysts can mediate fast, selective CO_2 reduction in a flow cell. *Science* **2019**, *365*, 367–369. [CrossRef]
51. Jouny, M.; Luc, W.; Jiao, F. High-rate electroreduction of carbon monoxide to multi-carbon products. *Nat. Catal.* **2018**, *1*, 748–755. [CrossRef]
52. Verma, S.; Hamasaki, Y.; Kim, C.; Huang, W.; Lu, S.; Jhong, H.-R.M.; Gewirth, A.A.; Fujigaya, T.; Nakashima, N.; Kenis, P.J.A. Insights into the low overpotential electroreduction of CO_2 to CO on a supported gold catalyst in an alkaline flow electrolyzer. *ACS Energy Lett.* **2017**, *3*, 193–198. [CrossRef]
53. Gao, Y.; Wu, Q.; Liang, X.; Wang, Z.; Zheng, Z.; Wang, P.; Liu, Y.; Dai, Y.; Whangbo, M.H.; Huang, B. Cu_2O nanoparticles with both {100} and {111} facets for enhancing the selectivity and activity of CO_2 electroreduction to ethylene. *Adv. Sci.* **2020**, *7*, 1902820. [CrossRef] [PubMed]
54. Hori, Y.; Takahashi, I.; Koga, O.; Hoshi, N. Electrochemical reduction of carbon dioxide at various series of copper single crystal electrodes. *J. Mol. Catal. A Chem.* **2003**, *199*, 39–47. [CrossRef]
55. Moller, T.; Scholten, F.; Thanh, T.N.; Sinev, I.; Timoshenko, J.; Wang, X.; Jovanov, Z.; Gliech, M.; Roldan Cuenya, B.; Varela, A.S.; et al. Electrocatalytic CO_2 reduction on CuO_x nanocubes: Tracking the evolution of chemical state, geometric structure, and catalytic selectivity using operando spectroscopy. *Angew. Chem. Int. Ed. Engl.* **2020**, *59*, 17974–17983. [CrossRef]
56. Biesinger, M.C.; Lau, L.W.M.; Gerson, A.R.; Smart, R.S.C. Resolving surface chemical states in XPS analysis of first row transition metals, oxides and hydroxides: Sc, Ti, V., Cu and Zn. *Appl. Surf. Sci.* **2010**, *257*, 887–898. [CrossRef]
57. Zeng, J.; Castellino, M.; Bejtka, K.; Sacco, A.; Di Martino, G.; Farkhondehfal, M.A.; Chiodoni, A.; Hernández, S.; Pirri, C.F. Facile synthesis of cubic cuprous oxide for electrochemical reduction of carbon dioxide. *J. Mater. Sci.* **2021**, *56*, 1255–1271. [CrossRef]
58. Biesinger, M.C. Advanced analysis of copper X-ray photoelectron spectra. *Surf. Interface Anal.* **2017**, *49*, 1325–1334. [CrossRef]
59. Peterson, A.A.; Nørskov, J.K. Activity descriptors for CO_2 electroreduction to methane on transition-metal catalysts. *J. Phys. Chem. Lett.* **2012**, *3*, 251–258. [CrossRef]
60. Singh, M.R.; Goodpaster, J.D.; Weber, A.Z.; Head-Gordon, M.; Bell, A.T. Mechanistic insights into electrochemical reduction of CO_2 over Ag using density functional theory and transport models. *Proc. Natl. Acad. Sci. USA* **2017**, *114*, E8812–E8821. [CrossRef]
61. Jedidi, A.; Rasul, S.; Masih, D.; Cavallo, L.; Takanabe, K. Generation of Cu–In alloy surfaces from $CuInO_2$ as selective catalytic sites for CO_2 electroreduction. *J. Mater. Chem. A* **2015**, *3*, 19085–19092. [CrossRef]
62. Zhong, D.; Zhao, Z.; Zhao, Q.; Cheng, D.; Liu, B.; Zhang, G.; Deng, W.; Dong, H.; Zhang, L.; Li, J.; et al. Coupling of Cu(100) and (110) facets promotes carbon dioxide conversion to hydrocarbons and alcohols. *Angew. Chem. Int. Ed. Engl.* **2020**, *60*, 4879–4885. [CrossRef]
63. Chang, I.C.; Chen, P.-C.; Tsai, M.-C.; Chen, T.-T.; Yang, M.-H.; Chiu, H.-T.; Lee, C.-Y. Large-scale synthesis of uniform Cu_2O nanocubes with tunable sizes by in-situ nucleation. *CrystEngComm* **2013**, *15*, 2363–2366. [CrossRef]
64. Kresse, G.; Hafner, J. Ab Initio molecular dynamics for liquid metals. *Phys. Rev. B Condens. Matter Mater. Phys.* **1993**, *47*, 558–561. [CrossRef]
65. Kresse, G.; Furthmuller, J. Efficiency of ab-initio total energy calculations for metals and semiconductors using a plane-wave basis set. *Comput. Mater. Sci.* **1996**, *6*, 15–50. [CrossRef]
66. Perdew, J.P.; Burke, K.; Ernzerhof, M. Generalized gradient approximation made simple. *Phys. Rev. Lett.* **1996**, *77*, 3865–3868. [CrossRef]
67. Kresse, G.; Joubert, D. From ultrasoft pseudopotentials to the projector augmented-wave method. *Phys. Rev. B Condens. Matter Mater. Phys.* **1999**, *59*, 1758–1775. [CrossRef]
68. Blochl, P.E. Projector augmented-wave method. *Phys. Rev. B Condens. Matter Mater. Phys.* **1994**, *50*, 17953–17979. [CrossRef]
69. Grimme, S.; Antony, J.; Ehrlich, S.; Krieg, H. A consistent and accurate ab initio parametrization of density functional dispersion correction (DFT-D) for the 94 elements H-Pu. *J. Chem. Phys.* **2010**, *132*, 154104. [CrossRef]
70. Mills, G.; Jonsson, H.; Schenter, G.K. Reversible work transition state theory: Application to dissociative adsorption of hydrogen. *Surf. Sci.* **1995**, *324*, 305–337. [CrossRef]
71. Henkelman, G.; Uberuaga, B.P.; Jónsson, H. A climbing image nudged elastic band method for finding saddle points and minimum energy paths. *J. Chem. Phys.* **2000**, *113*, 9901–9904. [CrossRef]
72. Henkelman, G.; Jónsson, H. A dimer method for finding saddle points on high dimensional potential surfaces using only first derivatives. *J. Chem. Phys.* **1999**, *111*, 7010–7022. [CrossRef]